Journal of Sound and Vibration 329 (2010) 5233–5248

Contents lists available at ScienceDirect

Journal of Sound and Vibration

journal homepage: www.elsevier.com/locate/jsvi

Control of a unique active vibration isolator with a phase compensation technique and automatic on/off switching

Gianmarc Coppola, Kefu Liu*

Department of Mechanical Engineering, Lakehead University, Thunder Bay, Canada

ARTICLE INFO

Article history:
Received 5 February 2010
Received in revised form
27 April 2010
Accepted 30 June 2010
Handling Editor: D.J. Wagg

ABSTRACT

This work examines the characteristics of a unique active vibration isolator and develops a control strategy for it. The proposed active vibration isolator is introduced and its dynamic model is presented. A characterization study is conducted to identify system parameters. It is shown that with a simple proportional feedback the closed-loop system has a very narrow stability margin due to the inherent dynamics of the actuator. To improve the stability of the closed-loop system and enhance the performance of vibration isolation, a phase compensator is incorporated in the control scheme. An optimization problem is formulated to determine the optimum controller parameters by minimizing the 2nd norm of the displacement transmissibility. Both absolute position feedback and relative position feedback are considered. In real time implementation, an automatic on/off switching strategy is devised to take full advantage of both the active isolator and passive isolator. The experimental results show that with the proposed control scheme, the isolator is capable of suppressing base excitations effectively.

1. Introduction

Methods to eliminate or isolate structural vibrations have been the topic of much research for several decades. Structural vibrations can occur in many different physical systems in a wide range of industries. Unaccounted for vibration transmission can cause instability or even failure, as is the case in buildings subject to earthquakes, or sensitive avionics mounted on the airframe of an aircraft for example [1]. The means to isolate vibration mainly include passive, semi-active or active control. In passive methodologies the isolation of any vibration-sensitive equipment from base excitation is achieved using resilient mounts [2]. However, conventional passive mounts suffer from an inherent trade-off between poor high-frequency isolation and amplification of vibration at the resonance frequency [3]. More recent passive mounts can incorporate a high stiffness, statically, to better support a larger load, and dynamically a very low stiffness to provide better isolation. This is known as a passive isolator with a high-static–low-dynamic stiffness (HSLDS) spring, which is capable of supporting a large load while possessing a low natural frequency [4–6]. A semi-active isolator can alter its stiffness or damping or both through a closed-loop system in order to improve isolation [7–12]. Some interesting semi-active control studies can be found in [13–15]. Also, active vibration isolators act by equipping the system with an actuator and a feedback control system to impose a controlled force on the structure. With proper design and control strategy, an active vibration isolator can deliver superior performance [16–22].

* Corresponding author. Tel.: +1 807 343 8634; fax: +1 807 343 8928.
E-mail address: kliu@lakeheadu.ca (K. Liu).

0022-460X/$ - see front matter © 2010 Elsevier Ltd. All rights reserved.
doi:10.1016/j.jsv.2010.06.025

In [23], a unique semi-active vibration isolator was developed. The proposed isolator possesses a HSLDS property that can be tuned both off-line and on-line. This paper presents a follow-up study. It shows that with a minor modification, the apparatus can also act as an active isolator. A dynamic system characterization is carried out in order to verify modeling and provide insight to unconsidered characteristics. A stability study is conducted to show that a simple proportional feedback control is not acceptable. A phase-lead compensation technique is utilized to improve the stability of the closed-loop system. Three controller parameters are identified. An optimization problem is formulated to determine the optimum controller parameters by minimizing the 2nd norm of the displacement transmissibility. Both absolute position feedback and relative position feedback are studied. In real time implementation, the best displacement transmissibility of the isolator is measured. An automatic on/off switching strategy is devised to take full advantage of both the active isolator and passive isolator. The experimental results show that with the proposed control scheme, the isolator is able to effectively suppress base excitations.

The rest of the paper is organized as follows. Section 2 presents the proposed active vibration isolator and its dynamic model. Section 3 addresses the system characterization. Section 4 develops a control strategy. Section 5 presents the experimental study results. Section 6 draws the conclusions for the study.

2. Active vibration isolator and dynamic models

Fig. 1 shows a schematic of the proposed active vibration isolator. A steel beam (1) is used to support a permanent magnet (PM) (2). The permanent magnet acts as an isolated mass and is referred to as mass denoted by m. The PM block is formed by two neodymium magnets enclosed in an aluminum casing. The block dimension is $l \times w \times h$=25.4 $\times 25.4 \times 29.0\ \mathrm{mm}^3$. Its magnetization is $786.23\ \mathrm{kA\,m^{-1}}$. The mass–beam assembly is placed between a pair of electromagnets (EMs) (3). The tension of the beam can be adjusted by screws (4). The beam supports and the EM supports are made of aluminum and they are fastened to an aluminum base which rides on two linear guide carts sliding along a precision rail rack (6). The rail rack is fastened to a heavy rigid stand (7). A shaker (5) is used to excite the base through a stinger.

Fig. 2 illustrates a simplified model for the system and indicates the polarities of the PM and the EMs. Note the two differences that distinguish the present setup from the one proposed in [23]. First the polarities of the EMs and PM for the present setup are such that a net force on the PM occurs as soon as the EMs are energized while the polarities of the EMs and PM for the setup in [23] are such that a net force on the PM occurs only when the PM is displaced away from its equilibrium position. Second the current to the EMs of the present setup is alternating while the current to the EMs of the setup in [23] is direct. Fig. 2 also defines some key variables used to describe the model. The base motion is denoted by y while the motion of the mass is denoted by x. The stiffness of the beam is represented by k_b while the stiffness of the magnetic spring due to the interaction between the PM and the EM cores is represented by k_{pc}.

The equation governing the motion of the mass is given by

$$m\ddot{z} + c\dot{z} + f_b + f_{pc} = -m\ddot{y} + F_c \tag{1}$$

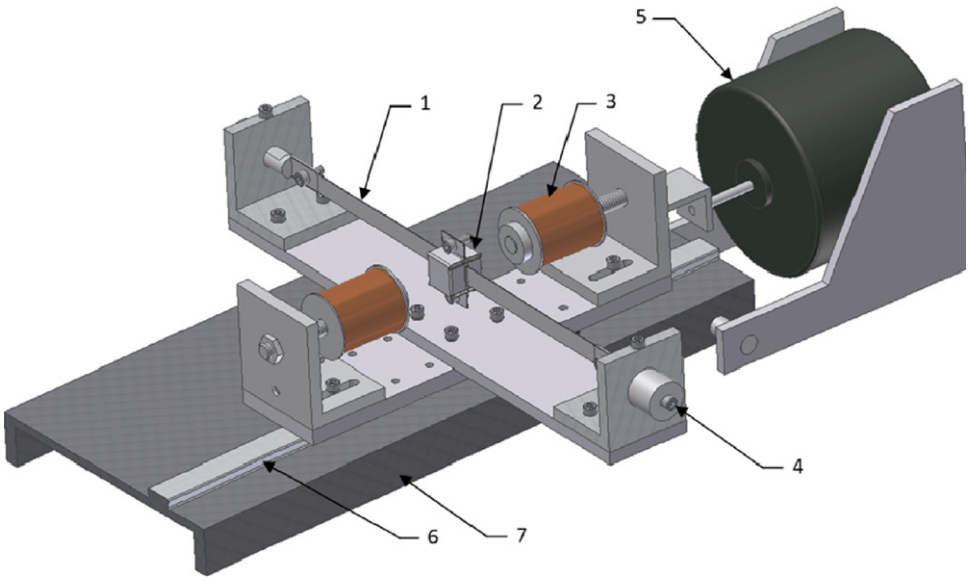

Fig. 1. Schematic of the active vibration isolator.

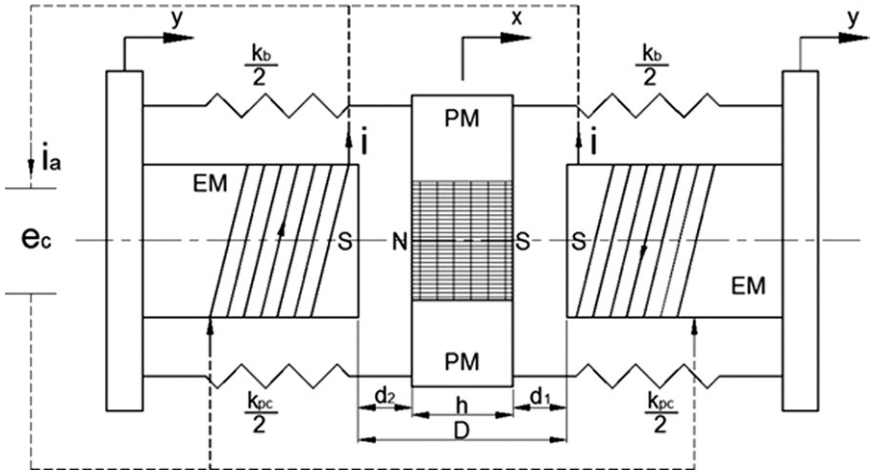

Fig. 2. Illustrative model.

where $z=x-y$ represents the relative displacement of the mass, f_b is the restoring force of the beam and f_{pc} is the attracting force of the magnetic spring, F_c is the actuating force due to the interaction between the PM and the energized EMs. The study conducted in [23,24] has found that the restoring force f_b can be approximated by a cubic function,

$$f_b = k_1 z + k_3 z^3 \tag{2}$$

where k_1 and k_3 are constant. In the Appendix, it is shown that the force due to the magnetic spring f_{pc} is given as

$$f_{pc} = -e^{-a_3|i|}\frac{8a_1q_1z(q_1^2+z^2)}{(q_1^2-z^2)^4} \tag{3}$$

and the actuating force is given as

$$F_c = sign(i)(1-e^{-b_3|i|})b_1\frac{2(q_2^4+6q_2^2z^2+z^4)}{(q_2^2-z^2)^4} \tag{4}$$

If the relative displacement z and the current i are small in magnitude, Eqs. (3) and (4) can be linearized such that

$$m\ddot{z}+c\dot{z}+(k_1-k_{pc})z = -m\ddot{y}+\gamma i_a \tag{5}$$

where $k_{pc}=8a_1/q_1^5$, $\gamma=b_1b_3/q_2^4$, and $i_a=2i$ is the total current applied to the actuator.

As shown in Fig. 2, the actuator is formed by connecting two identical EMs in parallel. Therefore, the dynamics of the actuator is defined by

$$\frac{L}{2}\dot{i}_a+\frac{R}{2}i_a+k_v\dot{z}=e_c \tag{6}$$

where L and R are the inductance and resistance of one EM, e_c is the voltage that is applied to the actuator, and the term $k_v\dot{z}$ represents the effect of back electromotive force (emf) induced by the motion of the mass with k_v as a proportional constant.

3. System characterization

Eqs. (5) and (6) are based on the simplified models. In order to control the system effectively, a thorough system characterization is needed. The characterization study serves a twofold purpose. While the primary purpose is to identify unknown dynamics/parameters and verify modeling, the study also intends to gain further insight to the limitations of the actual system and reveal any characteristics that are not included in the governing equations. Herein, an experimental approach was taken to characterize the system. The study employs a set of self-made electromagnets. Each of the electromagnets was constructed by winding 22 Gauge copper wire around a low-carbon steel bolt with a diameter of 13.0 mm. The outer diameter and length of the coil were both 55 mm, which results in about 1213 turns.

3.1. Electromagnet inductance

As shown in Eq. (6), the actuator dynamics involves the resistance R, the inductance L, and the constant k_v. Among them, the resistance is the easiest one to determine. Using a multimeter, it was found that the resistance for one EM was $R=8.2\ \Omega$. Thus, the study focuses on the determination of L and k_v. It is known that there are several factors that can affect the

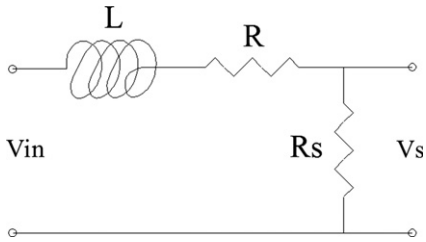

Fig. 3. Circuit used to measure the EM inductance.

inductance of a coil. These include temperature, current, frequency, magnitude, etc. [25,26]. Consequently, the correct inductance of an electromagnet should be determined in the domain of its use. Two methods were used for this purpose.

Step response method: Fig. 3 shows a depiction of a circuit that was used to determine the inductance of an electromagnet where L and R are the inductance and resistance of the coil, respectively and R_s=1 Ω is a resistor used to measure the current.

When a voltage v_{in} is applied to the circuit, the governing equation of the circuit is of the form:

$$L\dot{i}+(R+R_s)i=v_{in}(t) \tag{7}$$

If a constant voltage V is suddenly applied, the current can be found to be

$$i(t)=\frac{V}{R+R_s}(1-e^{-((R+Rs)/L)t}) \tag{8}$$

With knowledge of the resistance of the coil this equation can be used to estimate the inductance. In order to do so an experiment was conducted. The circuit was setup and a step voltage was applied to the amplifier (Quanser, UPM-2405) through the interface between dSpace Control Desk and Matlab Simulink. The corresponding current draw was measured. Subsequently, Eq. (8) can be broken down to estimate the inductance parameter. First, defining the time it takes for the current to reach exactly half of its final value starting at its initial value as $t_{1/2}$. Next, half of the final value of the current is given by $i_{1/2}=0.5V/(R+R_s)$. Using $t_{1/2}$ for t and $i_{1/2}$ for $i(t)$, Eq. (8) can be solved for the inductance L:

$$L=\frac{-(R+R_s)t_{1/2}}{\ln(1/2)} \tag{9}$$

From this point in the experiment, $t_{1/2}$ was obtained from the collected data. The experiments were repeated 3 times. The average inductance values were found to be L=0.16 H.

RLC resonance: The second method involved the resonance of an RLC circuit where the inductance is unknown. The governing differential equation for an RLC circuit is given by

$$L\ddot{i}+R\dot{i}+\frac{1}{C}i=\dot{v}(t) \tag{10}$$

where C is capacitance. The natural frequency of the system is the frequency at which the system experiences resonance. This is given by

$$\omega_n=\sqrt{\frac{1}{LC}} \tag{11}$$

Accordingly, an experiment was conducted to locate the natural frequency of the circuit by subjecting it to sinusoidal voltages with various frequencies. By measuring the magnitudes of the resulting currents, the relationship between the current magnitude and the exciting frequency can be established, where the frequency corresponding to the peak value is taken as the natural frequency of the circuit. Once this frequency was determined, Eq. (11) was used to find the inductance given the value of capacitance used in the experiment. This was done for 2 different sets of capacitors. This first had a capacitance value of 470 μF and the second 1000 μF. The experiments were repeated 3 times each. The average inductance values were found to be L=0.163 H. This value is close to the results obtained from the step response method. Hereinafter, the results from method one are utilized in the study.

3.2. Damping coefficient and the proportional constant for the back EMF term

When the PM moves between the EMs, eddy currents are induced in the EMs. These eddy currents create magnetic fields in the EMs that oppose the original magnetic field, thus causing a repulsive force onto the PM. This alters the damping coefficient c in Eq. (5). In the meantime, the PM motion also induces the back emf term $k_v\dot{z}$ in Eq. (6). The system characterization also involved the identification of c and k_v. A free response method was used to identify the damping coefficient c. For this purpose, the system was setup as shown in Fig. 1, an impact was applied to the PM and the free response was recorded. The recorded displacement that is truncated at its first peak can be considered to be a response

induced by an initial displacement $z(0)$ given by

$$z(t)=\frac{z(0)}{\sqrt{1-\zeta^2}}e^{-\zeta\omega_n t}\sin\left(\omega_n\sqrt{1-\zeta^2}t+\tan\left(\frac{\sqrt{1-\zeta^2}}{\zeta}\right)\right) \tag{12}$$

where $\omega_n=\sqrt{k/m}$ is the natural frequency and $\zeta=c/(2m\omega_n)$ is the damping ratio. Fig. 4 shows typical responses of the PM from the setup for three gap distances. By using $z(0)$ from the measured response and assigning trial values for ω_n and ζ, a response can be computed from Eq. (12). The root-mean-squared (rms) error between the experimental response and the computed response is found. A nonlinear optimization process was implemented to estimate the optimum values for ω_n and ζ such that the rms error is minimized. Table 1 lists the best estimated values for the damping coefficients. It is noted that with a decrease of the gap distance, the added damping increases.

Subsequently, the back emf proportional constant k_v was determined experimentally as well. The apparatus was setup as shown in Fig. 1 and the actuator circuit loop was closed. A sinusoidal excitation was generated to force the base of the apparatus into motion. The PM motion induced a current in the closed circuit. The current was measured directly. Fig. 5 shows typical induced currents. From Eq. (6), the voltage due to back emf was found by

$$v_{\text{emf}}=2k_v\dot{z}=-L\dot{i}_a-Ri_a \tag{13}$$

With the measured amplitude Z of the PM displacement and the known frequency ω, the proportional constant k_v can be found by

$$k_v=\frac{v_{\text{emf}}}{2\omega Z} \tag{14}$$

Table 1 lists the estimated values for k_v with three different gap distances. It is noted that with a decrease of the gap distance, the back emf effect increases.

3.3. Dynamic force identification

The actuating force model derived in the Appendix was based on the interacting force between a PM and an EM from static experiments for which constant currents were used [23,24]. It is expected that this model cannot accurately

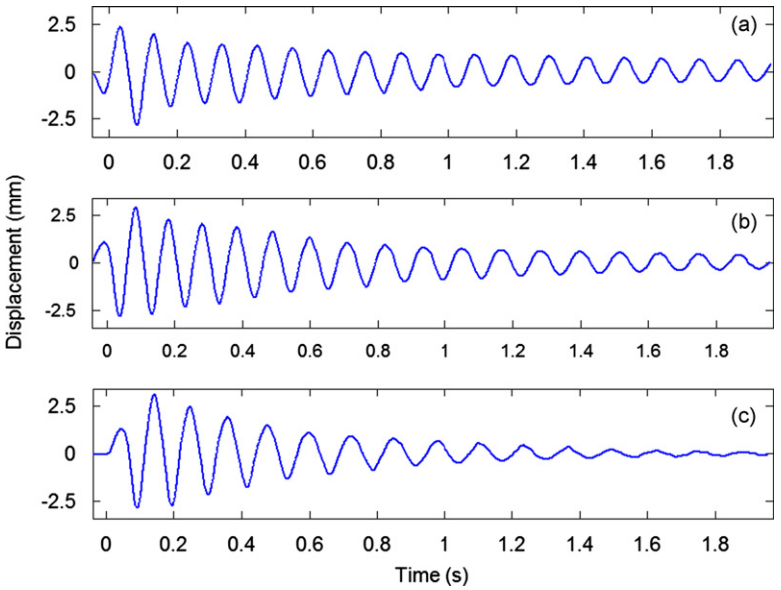

Fig. 4. Typical responses of the PM: (a) D=100 mm, (b) D=90 mm, and (c) D=80 mm.

Table 1
Estimated damping constants and back emf constants.

D (mm)	c (kg/s)	k_v (V s/m)
100	0.31	0.53
90	0.48	0.69
80	0.63	1.09

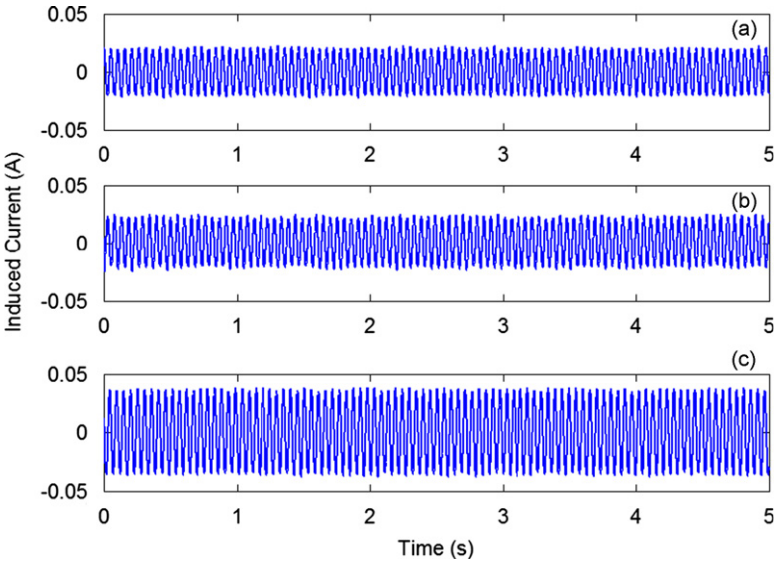

Fig. 5. Induced currents with ω=120 rad/s: (a) D=100 mm, (b) D=90 mm, and (c) D=80 mm.

represent an actuating force induced by alternating currents [27]. In order to gain a better understanding of the actuating force, a dynamic force identification was conducted. One method to obtain the dynamic force is via state measurement directly from experiment. Subsequently, the states can be directly used in the dynamic model to estimate the force produced. In order to reduce the nonlinearity effect, the beam was replaced by a cantilever beam whose stiffness is more linear than that of the actual beam. The governing equation of this setup is given by

$$m_b\ddot{z}+c_b\dot{z}+k_bz=F(t) \tag{15}$$

where through an experimental identification, it was found that m_b=0.14 kg, c_b=0.572 kg/s, and k_b=2800 N/m. With the apparatus base firmly fixed, a sinusoidal current $i(t)=I_0\sin(\omega t)$was applied to the actuator and the steady-state displacement of the mass was measured. If it is assumed that $F(t)=F_0\sin(\omega t)$, the steady-state response of the mass is given by

$$(-\omega^2m_b+j\omega c_b+k_b)Z(j\omega)=F(j\omega) \tag{16}$$

or

$$F_0=|Z(j\omega)|m_b\sqrt{(\omega_n^2-\omega^2)^2+(2\omega\omega_n\zeta)^2} \tag{17}$$

where $\omega_n=\sqrt{k_b/m_b}$ and $\zeta=c_b/(2m_b\omega_n)$. From Eq. (17), the dynamic force amplitude F_0 can be evaluated. Various experiments were conducted in which currents with various amplitudes and frequencies were applied and the steady-state responses of the mass were measured.

Fig. 6 shows the dynamic force amplitudes generated by the experiment. A few observations can be made. First, the proportionality of the force amplitude vs. the current amplitude exists only when the current amplitude is small. Second, the force amplitude is a function of the exciting frequency; the higher the exciting frequency, the smaller the force amplitude. According to the simplified force model, the actuating force is proportional to the current with the proportional constant given by $\gamma=b_1b_3/q_2^4$ where $q_2=(D-h)/2+b_2$. The effect of the gap distance on the dynamic force amplitude was investigated as well. Fig. 7 compares the dynamic force amplitudes for three different gap distances. The results indicate that the greater the gap distance, the smaller the dynamic force amplitude.

4. Stability analysis and control design

The notion of stability analysis arises from the knowledge that the system under consideration possesses some unique attributes that make active control challenging. Moreover, the main idea behind a linear stability analysis of such a system is that the dynamics of the nonlinear system near a hyperbolic equilibrium point can be determined from a linearization about that equilibrium point. For this purpose, Eqs. (5) and (6) are repeated below

$$\begin{aligned} m\ddot{z}+c\dot{z}+kz&=\gamma i_a\\ L\dot{i}_a+Ri_a+2k_v\dot{z}&=2e_c \end{aligned} \tag{18}$$

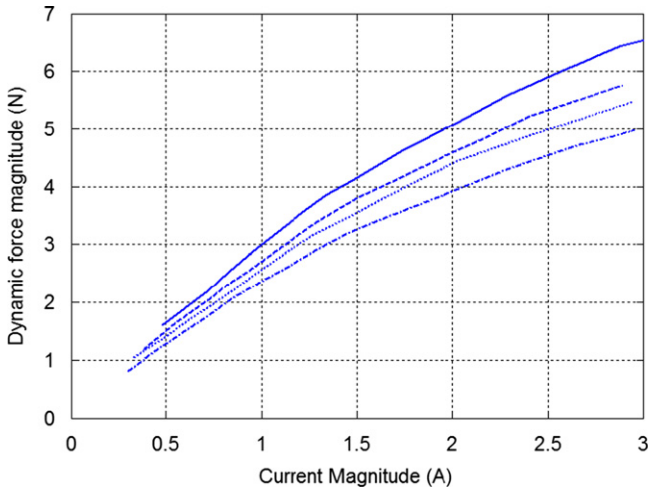

Fig. 6. Dynamic force for various frequencies at D=100 mm: ω=30 rad/s (solid line), ω=60 rad/s (dashed line), ω=80 rad/s (dotted line), and ω=100 rad/s (dash-dot line).

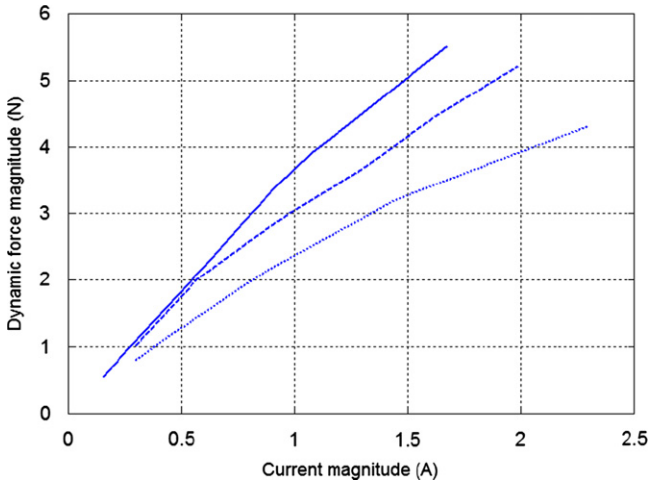

Fig. 7. Dynamic force amplitudes with ω=100 rad/s: D=100 mm (dotted line), D=90 mm (dashed line), and D=80 mm (solid line).

Table 2
The parameter values used in the stability analysis.

Mechanical system	Actuator
m=0.17 kg k=754 N/m c=0.31 kg/s	γ=2.46 N/A L=0.16 H R=9.2 Ω k_v=0.53 V s/m

with $k=k_1-k_{pc}$. Table 2 lists the parameter values used in the stability study. It is important to note that all the values except γ were identified using the setup shown in Fig. 1 with the EM gap distance set at D=100 mm. The value for γ was determined using the results from Section 3.3 in the following way. First, the force–current relationship was obtained using the exciting frequency ω=66.02 rad/s that is equal to the natural frequency of the passive isolator. Then the slope of the force–current curve was found by a linear interpolation. The found slope was used as an approximate value for γ.

A proportional feedback is considered. In practice, there are two permissible ways to introduce a proportional feedback: absolute position feedback (APF) and relative position feedback (RPF) [28]. Although the latter is not as common as the former, it has been used in conjunction with other control sequences as in [29]. For the APF, the control voltage applied to

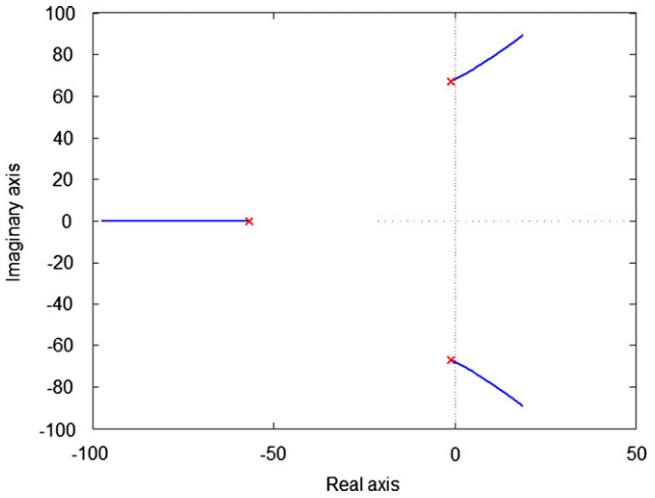

Fig. 8. Root loci of the closed-loop system with the proportional control.

the actuator is given by $e_c = -K_p x$ whereas for the RPF, $e_c = -K_p z$ where K_p is the feedback gain. For both the APF and the RPF, the characteristic equation of the closed-loop system is given by

$$s^3 + \left(\frac{R}{L} + \frac{c}{m}\right)s^2 + \left(\frac{Rc}{mL} + \frac{k}{m} + \frac{2\gamma k_v}{mL}\right)s + \frac{kR}{mL} + \frac{2\gamma K_p}{mL} = 0 \tag{19}$$

where s is a complex number.

The root loci of Eq. (19) can be seen in Fig. 8. It is quite evident that the system starts out marginally stable for a low gain, and then quickly becomes unstable as the gain increases. The crossing gain is the proportional gain at which the root loci cross the imaginary axis from the left-hand plane to the right-hand plane. The crossing gain corresponding to Fig. 8 was $K_p = 104$, which is too small to generate a sufficient control force. From this analysis the direct proportional feedback control is deemed unsatisfactory.

4.1. Phase compensation technique—absolute position feedback (APF)

The inherent instability of the closed-loop system is mainly due to the phase lag caused by the dynamics of the actuator. One of the common solutions to the problem is to incorporate a phase compensator [30–32]. This approach was investigated in this study. The objective is to design a phase-lead compensator so that the stability and performance of the overall closed-loop system is improved. The transfer function of the phase compensation network is given by

$$G_c(s) = \frac{s + 1/T}{s + 1/(\alpha T)} \tag{20}$$

where $\alpha = R_2/(R_1 + R_2)$ and $T = R_1 C_1$. Fig. 9 shows the block diagram for the closed-loop system that incorporates the phase compensator with the absolute position feedback.

The displacement transmissibilty is given by

$$TR(\omega) = \left|\frac{X(\omega)}{Y(\omega)}\right| = \left|\frac{cLs^2 + (cR + kL + 2\gamma k_v)s + kR}{mLs^3 + (mR + cL)s^2 + (cR + kL + 2\gamma k_v)s + kR + 2\gamma K_p G_c(s)}\right|_{s = j\omega} \tag{21}$$

where $X(\omega)$ is the amplitude of the steady-state response of the mass and $Y(\omega)$ is the amplitude of the harmornic base excitation. There are three parameters to be determined: T, α, and K_p. An optimization problem is formulated in order to find the best parameter values. The optimum parameter values should be chosen so as to minimize the following objective function:

$$f = ||TR(\omega)||_2 \text{ in the frequency range } 0 \le \omega \le \omega_u$$

where $\|\bullet\|_2$ denotes the second norm and ω_u is a prescribed upper bound for the frequency of interest. The optimization is subjected to the following constraints:

1. The poles of the characteristic equation of the closed-loop system must lie on the left-hand side of the complex plane or the closed-loop system is stable.
2. $T_l \le T \le T_u$, $\alpha_l \le \alpha \le \alpha_u$, $K_{pl} \le K_p \le K_{pu}$
   where T_l, α_l, K_{pl} and T_u, α_u, K_{pu} are the lower bounds and the upper bounds of the parameters, respectively. The sequential simplex algorithm was used in the numerical solution.

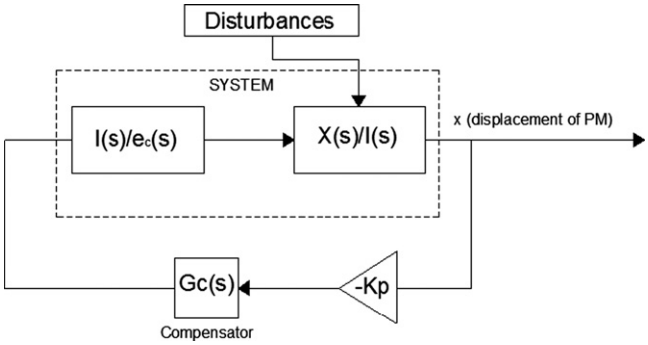

Fig. 9. Block diagram of the APF with the phase compensation.

Table 3
The parameters of the optimum controllers with the APF.

	K_{pu}	K_p^*	T^*	α^*
Controller one	50,000	4.9962×10^4	3.8356	3.8412×10^{-4}
Controller two	100,000	9.9998×10^4	2.3963	4.5600×10^{-4}
Controller three	150,000	1.4999×10^5	1.9772	4.6512×10^{-4}

The frequency upper bound was prescibed to be ω_u=200 rad/s and the parameter bounds were T_l=0.025, $\alpha_l=5\times10^{-5}$, K_{pl}=7000 and T_u=10, $\alpha_u=5\times10^{-3}$. For the upper bound of the feedback gain, three values were perscribed and they are given in Table 3. Numerous computations were conducted. Table 3 lists the parameters of the three optimum controllers. Fig. 10 compares the *TR*s obtained by the optimum controllers with the *TR* obtained by the passive isolator. Several observations can be drawn:

1. The active control greatly improves the *TR* in the lower frequency region and suppresses the *TR* at the resonance frequency of the original system.
2. Around the resonance freuquency of the closed-loop system, *TR* with control is greater than that without control, which means that, in such a frequency range, the passive isolator outperforms the active one.
3. The optimum feedback gain K_p always converges to the prescribed upper bound, which indicates that the higher the feedback gain, the smaller the resulting objective function.

Fig. 11 illustrates the root loci of the closed-loop systems with the optimum controllers. The asterisks designate the points that correspond to the optimal gains. Evidently, the system is now asymptotically stable for the optimum gains. The effect of the increased upper bound on K_p can also be observed. Clearly, as the upper bound on K_p increases the effect that the compensator imposes on the systems character is more drastic, effectively pulling the roots further away from the imaginary axis.

4.2. Phase compensation technique—relative position feedback (RPF)

For the RPF, the displacement transmissibility is given by

$$TR(\omega)=\left|\frac{X(\omega)}{Y(\omega)}\right|=\left|\frac{cLs^2+(cR+kL+2\gamma k_v)s+kR+2\gamma K_pG_c(s)}{mLs^3+(mR+cL)s^2+(cR+kL+2\gamma k_v)s+kR+2\gamma K_pG_c(s)}\right|_{s=j\omega} \tag{22}$$

In the same manner as Section 4.1 the controller parameters were obtained by optimizing the 2nd norm of the transmissibility in the base excitation frequency region from 0 to 200 rad/s.

Numerical solutions were conducted. It was found that increasing the upper bound on the gain did not have a significant effect on the results. Only if the upper bound was increased very drastically did the results have a noticeable change. Thus, the upper bound for the gain was set to be $K_{pu}=5\times10^4$. Fig. 12 compares the *TR* of the passive isolator and the *TR* of the optimal active isolator with the RPF. Notable differences between the APF and the RPF can be observed. Firstly, in a general sense the APF performs better than the RPF. Both the APF and the RPF are able to isolate vibration at frequencies around the natural frequency of the open-loop system, but the APF results in $TR<1$ for a low to middle frequency range, whereas the RPF cannot provide such results. Also, the natural frequency of the closed-loop system with the RPF is lower than that with the APF.

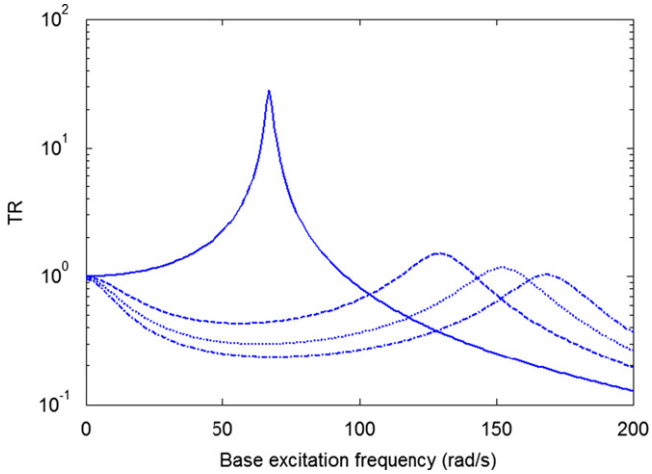

Fig. 10. Comparison of the *TR* of the passive isolator and the *TRs* of the optimum active isolators with the APF: the passive isolator (solid line), controller one (dashed line), controller two (dotted line), and controller three (dash-dotted line).

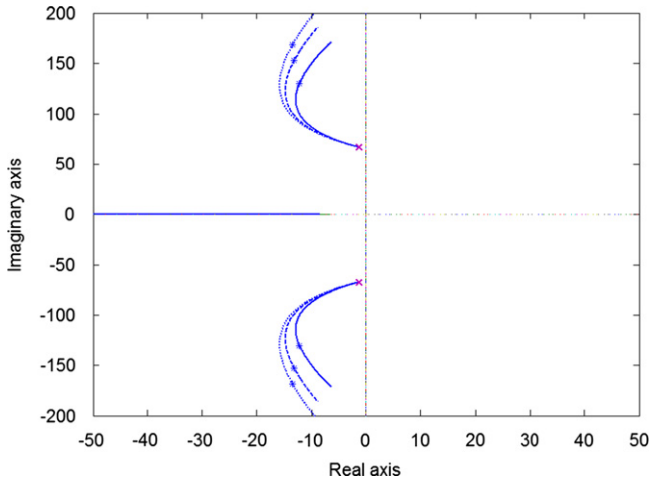

Fig. 11. Root loci of the closed-loop systems with actuator, using the APF: with controller one (solid line), with controller two (dashed line), and with controller three (dotted line).

5. Real time implementation

An experimental study was conducted in order to test the effectiveness of the proposed control strategy for the active vibration isolator. The system was tested with a gap distance of D=100 mm. The experiments included two parts. The first part consisted of determining the best displacement transmissibility. This was done by subjecting the base to a sinusoidal excitation and measuring the steady-state responses of both the mass and base. The second part developed an automatic on/off control such that the control system is capable of deciding whether the active control is needed or not. A personal computer equipped with a data acquisition (DAQ) board (dSpace 1104) was used to collect signals and to generate control inputs. Simulink was used in conjunction with dSpace Control Desk software in order to implement the control. A sampling frequency of 1000 Hz was used in the real time implementation. Only the results using the APF are reported.

Fig. 13 shows a Simulink real time model used in the first part of the experimental study. A laser position sensor (Wenglor, CP24MHT80) was used to measure the absolute displacement of the mass through ADC_C5 (analog-to-digital conversion). The signal was subtracted from a set point which was the equilibrium position of the mass. This position difference was fed into the optimal phase compensator. The output of the phase compensator was multiplied by the optimal gain before being sent out to DAC_C5 (digital-to-analog conversion). DAC_C5 being the channel connected directly to the power amplifier (Quanser, UPM-2405) that drives the actuator. A manual switch was used to control whether to activate the active control or not. Two accelerometers (Brüel & Kjær, 4393 V), one placed on the mass and one on the base were used to measure the acceleration signals. The acceleration of the base was acquired through ADC_C8 while the

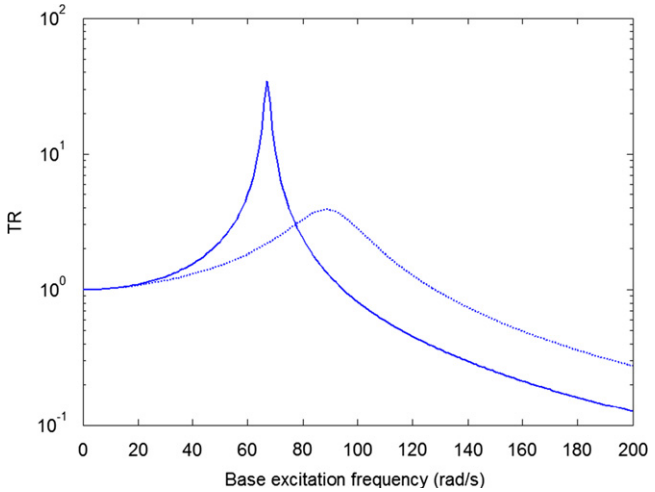

Fig. 12. Comparison of the *TR* of the passive isolator and the *TR* of the optimum active isolators with the RPF: passive isolator (solid line), active isolator with $K_p^* = 4.9994 \times 10^4$, T=5.4497, and $\alpha^* = 8.8062 \times 10^{-5}$ (dotted line).

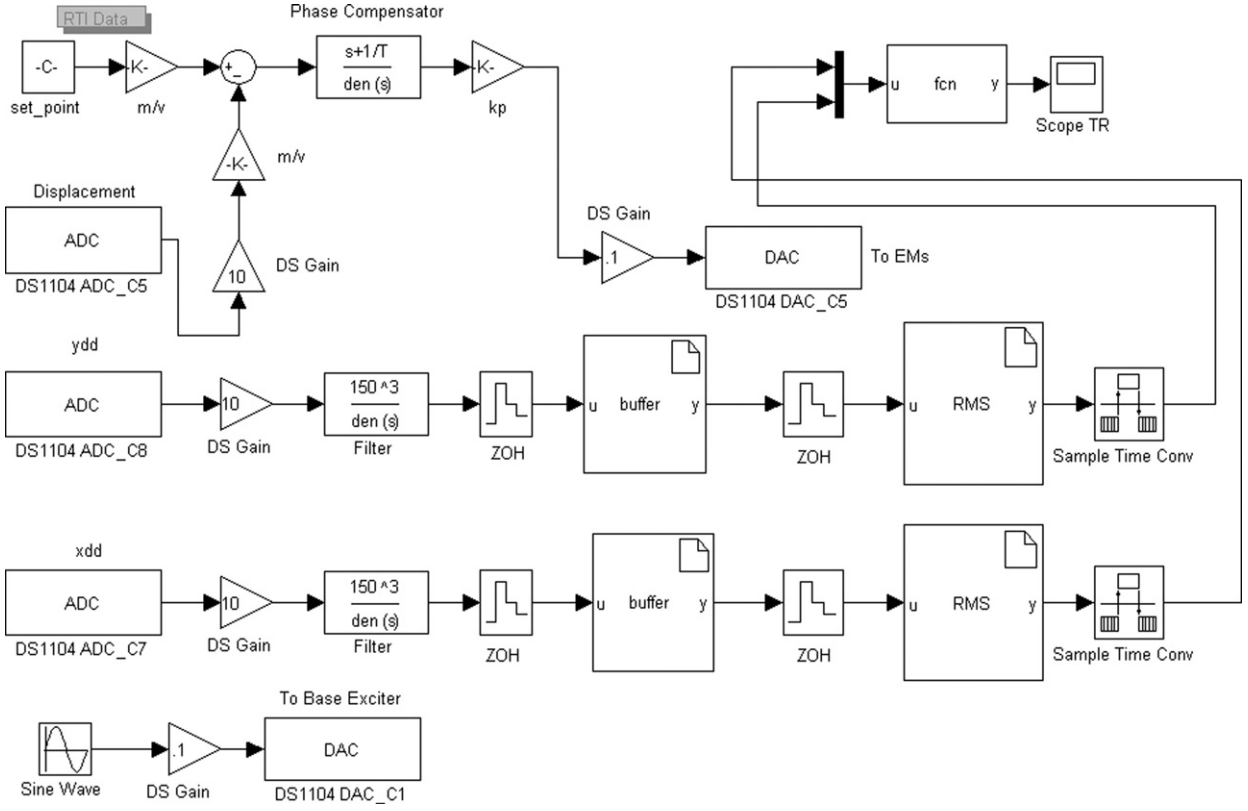

Fig. 13. Simulink real time model for measuring *TR*.

acceleration of the mass through ADC_C7. Each of the sampled acceleration signals was fed to a low-pass filter with a cut-off frequency of 23.87 Hz or 150 rad/s. An *S*-function "buffer" was used to collect a group of 2048 samples. Next, an *S*-function "rms" was used to compute the rms value of the 2048 samples. The displacement transmissibility was computed by dividing the rms value of the mass acceleration signals by the rms value of the base acceleration signals. This could be done on-line or off-line. A sinusoidal signal generated by a sin function generator was fed to DAC_C1. The output signal from DAC_C1 was fed into a power amplifier (Brüel & Kjær, 2706) to drive a shaker (Brüel & Kjær, 4809) that was used to excite the base.

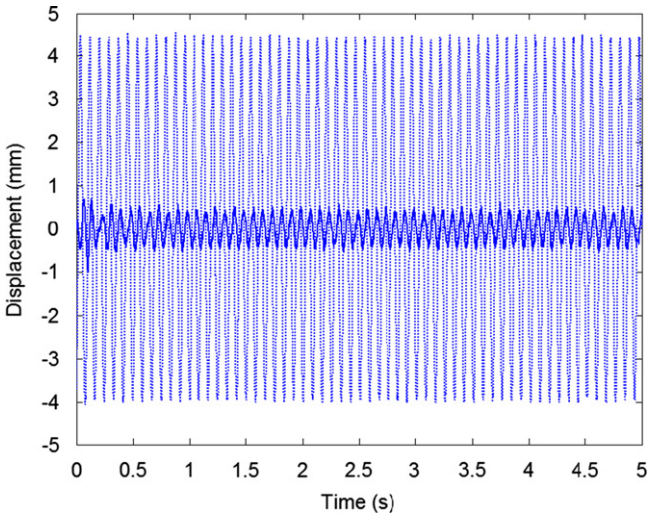

Fig. 14. Response of the mass to a sinusoidal base excitation (ω=75 rad/s): without control (dotted line) and with control (solid line).

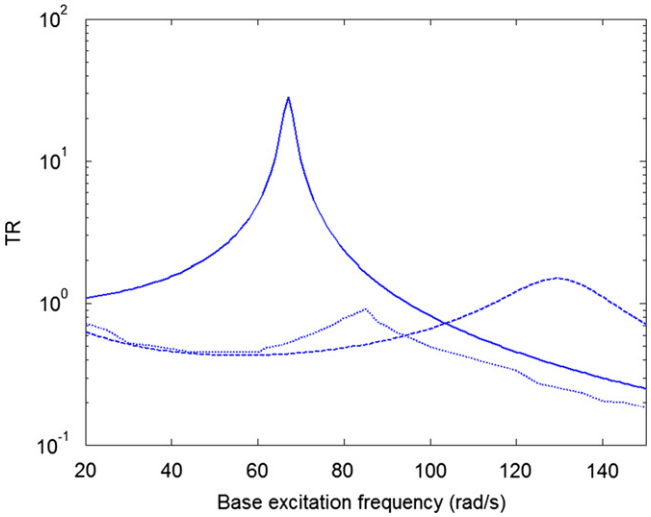

Fig. 15. *TRs*: analytical *TR* for the passive isolator (solid line), analytical *TR* with control (dashed line), and best experimental *TR* (dotted line).

Figs. 14 and 15 show some typical experimental results. Fig. 14 compares the time responses without control and the ones with control. Fig. 15 compares three *TRs* where the experimental *TR* was the best performance achieved by the isolator either in the active mode or in the passive mode. The frequency corresponding to the peak in the experimental *TR* is referred to as the switching frequency in this study. When the exciting frequency was below the switching frequency, the isolator was in its active mode; otherwise the isolator was in its passive mode. The results show that the active control was able to significantly suppress the base excitation, isolating the mass.

A need for an automatic switch control arises due to the fact that the active isolator performs better than the passive vibration isolator only in a low to middle frequency range. This requires that the control system be able to activate the active control only when it is needed. If the dominant frequency present in the response is smaller than the switching frequency, the active control should be activated. Otherwise, the control should be switched off. Fig. 16 shows a Simulink model that implements an automatic on/off control.

For the implementation of the automatic on/off control, the displacement signal from ADC_C5 was utilized both to generate a control effort and to determine whether to activate the control effort or not. The fast Fourier transform (FFT) was used to determine the dominant frequencies in the response from a collected 2048 samples. To do so, a group of the 2048 samples was collected with an *S*-function named "buffer" and then the 2048 samples were sent to an *S*-function named "FFT". The output of this *S*-function was the two frequencies corresponding to the first two highest peaks in the FFT spectrum, namely the primary and the secondary frequencies. These two frequencies were then sent to an embedded

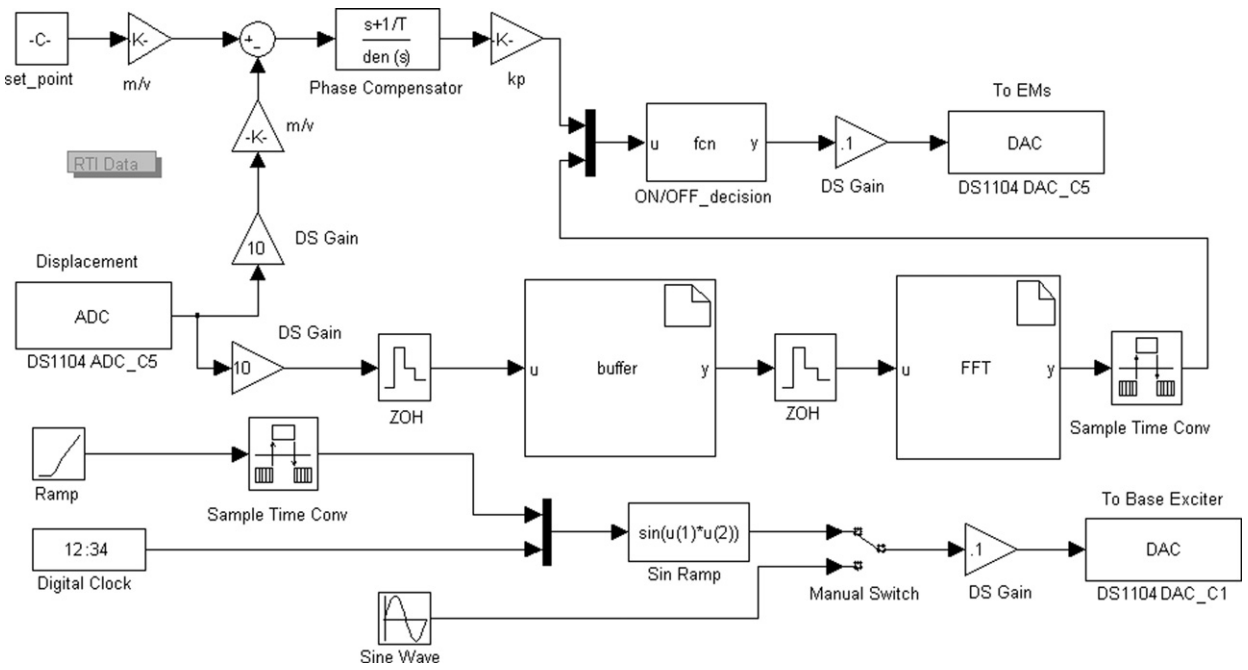

Fig. 16. Simulink real time model for automatic on/off control.

function named ''ON/OFF_decision'' where a decision was made on which of the dominant frequencies was the excitation frequency. In most cases, the primary dominant frequency corresponded to the excitation frequency. However, there is a case in which the secondary dominant frequency is the actual excitation frequency. This happens when the response is dominated by a transient. A transient occurs whenever the operating condition alters. For instance, a transient response is induced when the exciting frequency varies or when the system switches between the active mode and the passive mode. It was observed that only when the frequency of the transient was very close to the natural frequency of the passive isolator, the transient became dominant. Therefore, in ''ON/OFF_decsion'', the primary and secondary frequencies were compared to the predetermined natural frequency. In general, if the difference between the primary frequency and the natural frequency of the passive isolator was within the prescribed bound, then the secondary frequency was taken as the exciting frequency. Once the excitation frequency was determined, the following rules were applied: If the excitation frequency was less than or equal to the switching frequency then the active control strategy was activated, or kept on if it was already on. If the excitation frequency was greater than the switching frequency then the active control strategy was switched off, or kept off if it was already off. In this manner, about every 2 s the excitation frequency was updated and compared with the switching frequency. In the following, only the results with the APF are presented. In this case, the switching frequency is 82 rad/s as indicated in Fig. 15.

In order to illustrate the effectiveness of the on/off switching control in dealing with variable exciting frequencies, two testing scenarios were devised. The first scenario consisted of a multi-step change in the excitation frequency, and the second consisted of a linear ramped up change in the excitation frequency. The experimental results for the first scenario can be seen in Fig. 17. The step changes were as follows. For $0 \leq t < 10$ s the excitation frequency was 60 rad/s. Then at $t=10$ s the excitation frequency was changed to 70 rads/s. Then at $t=20$ s the excitation frequency was changed to 85 rad/s and followed by a final change at $t=35$ s to a frequency of 60 rad/s. Without control, the response of the mass increased with time and reached maximum amplitude when the excitation frequency was around the resonant frequency. After the exciting frequency surpassed the resonant frequency, the response started to decrease. With control, the response of the mass was kept at a low magnitude. Also, just before 25 s the automatic switch recognized the need to switch off the active control effort, resulting in a response similar to that of the passive isolator. It also recognized the need to switch the active controller back on just before 40 s.

For the linear ramp up scenario, the excitation frequency was linearly varied from 20 to 120 rad/s between 0 and 50 s. The results for this scenario can be seen in Fig. 18. Evidently, without control the system response increased drastically through resonance and then dropped subsequently. With the proposed control action the system responded with minimal vibration through the entire frequency range. The automatic on/off switch control was successful in switching off the control when the frequency of excitation reached the switching frequency. It was also successful in recognizing the transient that the system exhibited when the control was switch off. This can be observed around 35 s in Fig. 18 where the secondary frequency was correctly chosen as the excitation frequency.

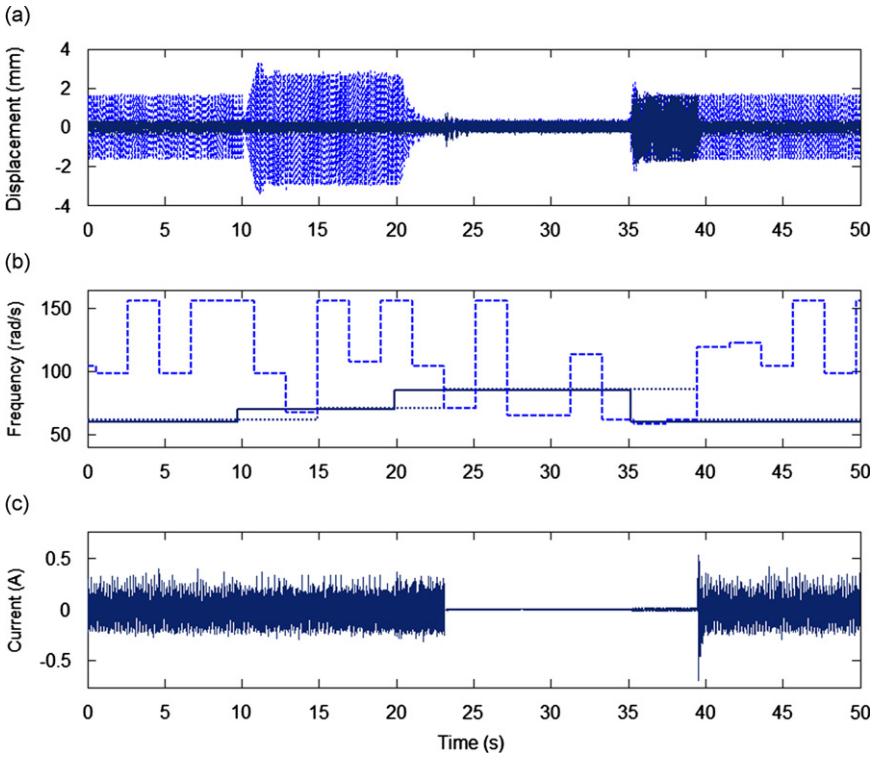

Fig. 17. Experimental results, multi-step change: (a) response of the mass without control (dashed line), with control (solid line); (b) base excitation frequency (solid line), measured primary frequency (dotted line), measured secondary frequency (dashed line); and (c) current of the actuator.

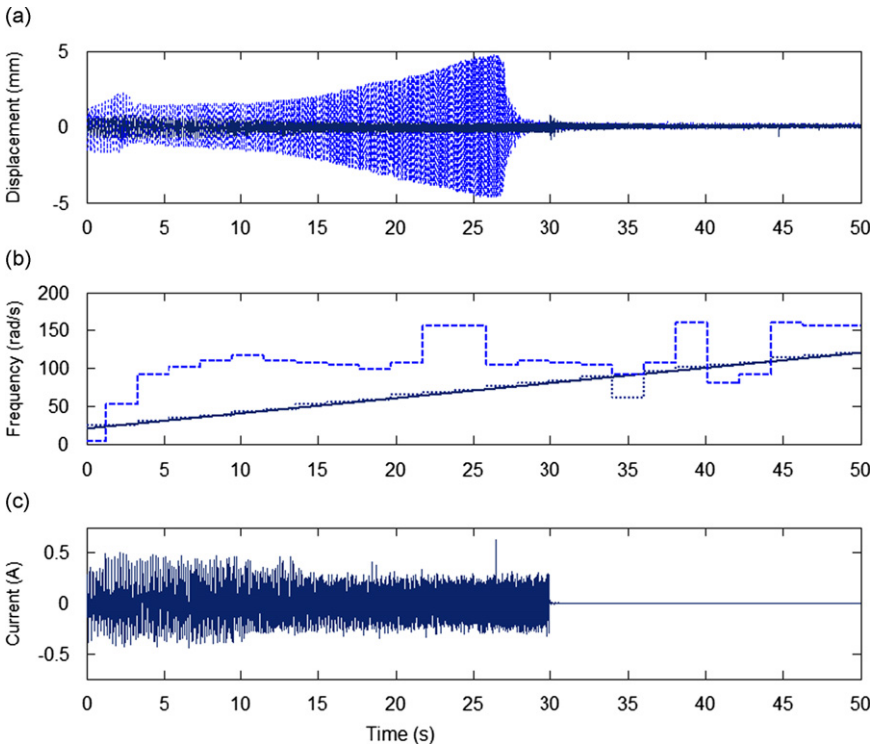

Fig. 18. Experimental results, linear ramp change: (a) response of the mass without control (dashed line), with control (solid line); (b) base excitation frequency (solid line), measured primary frequency (dotted line), measured secondary frequency (dashed line); and (c) current of the actuator.

6. Conclusions

In this paper, a unique active vibration isolator and its control strategy have been developed. The linearized dynamic models for both the mechanical system and the actuator have been presented. A system characterization has been conducted in order to identify the system parameters and reveal dynamics otherwise neglected in the linear models. The stability study has shown that the proportional feedback has a narrow stability margin due to the inherent dynamics of the actuator. A phase-lead compensator has been employed to improve the stability of the closed-loop system. An optimization problem has been formulated to determine the optimum parameters for the controllers by minimizing the second norm of the displacement transmissibility. Both the absolute position feedback and relative position feedback have been considered. The optimization results have shown that with the optimum controller and the absolute position feedback, the active vibration absorber can effectively isolate base excitation in a low to middle frequency range. An experimental study has been conducted. The best displacement transmissibility of the isolator has been determined experimentally. An on/off switching control strategy has been devised to take full advantage of both the passive isolator and active isolator. The testing results have demonstrated the effectiveness of the on/off switching control.

A final note is made on the potential applications of the proposed active vibration isolator. Although the present work is a proof of concept study, several potential applications are under consideration. For example, the proposed unit can be used to develop a vibration isolation table or to improve the comfort of a vehicle driver's seat. Of course, to realize these goals, several practical issues must be addressed. They include unit miniature and efficiency, etc. These remain to be investigated in a future study.

Appendix. Electromagnetic force model

Firstly, consider the interaction force between only one of the EMs and the PM. According to the study conducted in [23,24], this force consists of two parts:

$$F = F_{pc} + F_{pf} \tag{A1}$$

where F_{pc} denotes an attracting force between the core of the EM and the PM and F_{pf} the force due to the interaction between the PM and the flux generated by the energized EM. It was found that F_{pc} and F_{pf} can be expressed as

$$F_{pc} = e^{-a_3|i|}\frac{a_1}{(d+a_2)^4} \tag{A2}$$

and

$$F_{pf} = sign(i)(1-e^{-b_3|i|})\frac{b_1}{(d+b_2)^4} \tag{A3}$$

respectively, where d denotes the distance between the PM and the EM, i is the current in the EM, $sign(i)=1$ if $i>0$, $sign(i)=-1$ if $i<0$, and a_1, a_2, b_1, b_2, and b_3 are constants that depend on the setup and can be determined experimentally. For the present apparatus shown in Fig. 1, if the PM is displaced by a distance z, the total force on the PM becomes

$$F = F_{pc}(d_1) - F_{pc}(d_2) + F_{pf}(d_1) + F_{pf}(d_2) \tag{A4}$$

where

$$d_1 = \frac{D-h}{2} - z, \quad d_2 = \frac{D-h}{2} + z \tag{A5}$$

Substituting Eqs. (A2) and (A3) in Eq. (A4) yields

$$\begin{aligned} F &= e^{-a_3|i|}a_1\left[\frac{1}{(q_1-z)^4} - \frac{1}{(q_1+z)^4}\right] + sign(i)(1-e^{-b_3|i|})b_1\left[\frac{1}{(q_2-z)^4} + \frac{1}{(q_2+z)^4}\right] \\ &= e^{-a_3|i|}\frac{8a_1q_1z(q_1^2+z^2)}{(q_1^2-z^2)^4} + sign(i)(1-e^{-b_3|i|})b_1\frac{2(q_2^4+6q_2^2z^2+z^4)}{(q_2^2-z^2)^4} \end{aligned} \tag{A6}$$

where

$$q_1 = \frac{D-h}{2} + a_2, \quad q_2 = \frac{D-h}{2} + b_2 \tag{A7}$$

The first term on the right-hand side of Eq. (A6) represents the difference in the attracting force. This term can be linearized as

$$e^{-a_3|i|}a_1\left[\frac{1}{(q_1-z)^4} - \frac{1}{(q_1+z)^4}\right] \approx (1-a_3|i|)a_1\left[\frac{1}{q_1^4} + \frac{4}{q_1^5}z - \frac{1}{q_1^4} + \frac{4}{q_1^5}z\right] = (1-a_3|i|)\frac{8a_1}{q_1^5}z. \tag{A8}$$

The second term on the right-hand side of Eq. (A6) represents the sum of the actuating force generated by the energized EMs. This term can be linearized as

$$sign(i)(1-e^{-b_3|i|})b_1\left[\frac{1}{(q_2-z)^4}+\frac{1}{(q_2+z)^4}\right]\approx sign(i)(1-1+b_3|i|)b_1\left[\frac{1}{q_2^4}+\frac{4}{q_2^5}z+\frac{1}{q_2^4}-\frac{4}{q_2^5}z\right]=\frac{b_1b_3}{q_2^4}2i \tag{A9}$$

It is further assumed that the influence of the coil current on the interacting force between the PM and the EM cores can be neglected or $(1-a_3|i|)\approx 1$. Thus the linearized interacting force is given by

$$F=\frac{8a_1}{q_1^5}z+\frac{b_1b_3}{q_2^4}2i \tag{A10}$$

The first term on the right-hand side of the above equation depends on the displacement of the PM, which indicates that the interacting force between the PM and the EM cores acts as a negative spring. The second term on the right-hand side of the above equation indicates that the actuating force is proportional to the current and inversely proportional to D^4.

References

[1] A.H. El-Sinawi, Active vibration isolation of a flexible structure mounted on a vibrating elastic base, *Journal of Sound and Vibration* 271 (2004) 323–337.
[2] L. Benassi, S.J. Elliott, P. Gardonio, Active vibration isolation using an inertial actuator with local force feedback control, *Journal of Sound and Vibration* 276 (2004) 157–179.
[3] X. Huang, S.J. Elliott, M.J. Brennan, Active isolation of a flexible structure from base vibration, *Journal of Sound and Vibration* 263 (2003) 357–376.
[4] R.A. Ibrahim, Recent advances in nonlinear passive vibration isolators, *Journal of Sound and Vibration* 314 (2008) 371–452.
[5] A. Carrella, M.J. Brennan, T.P. Waters, Static analysis of a passive vibration isolator with quasi-zero-stiffness characteristic, *Journal of Sound and Vibration* 301 (2007) 678–689.
[6] I. Kovacica, M.J. Brennan, T.P. Waters, A study of a nonlinear vibration isolator with a quasi-zero stiffness characteristic, *Journal of Sound and Vibration* 315 (2008) 700–711.
[7] Y. Liu, T.P. Waters, M.J. Brennan, A comparison of semi-active damping control strategies for vibration isolation of harmonic disturbances, *Journal of Sound and Vibration* 280 (2005) 21–39.
[8] Y. Liu, T.P. Waters, M.J. Brennan, Semi-active vibration isolation system with variable stiffness and damping control, *Journal of Sound and Vibration* 313 (2008) 16–28.
[9] J.M. Cronje, P.S. Heyns, N.J. Theron, P.W. Loveday, Development of a variable stiffness and damping tunable vibration isolator, *Journal of Vibration and Control* 11 (2005) 381–396.
[10] Y. Nitta, A. Nishitani, B.F. Spencer Jr, Semi-active control strategy for smart base isolation utilizing absolute acceleration information, *Structural Control and Health Monitoring* 13 (2006) 649–659.
[11] Z. Xu, A.K. Agrawal, J.N. Yang, Semi-active and passive control of the phase I linear base-isolated benchmark building model, *Structural Control and Health Monitoring* 13 (2006) 626–648.
[12] D.A. Shook, P.N. Roschke, O.E. Ozbulut, Superelastic semi-active damping of a base-isolated structure, *Structural Control and Health Monitoring* 15 (2008) 746–768.
[13] F. Casciati, M. Domaneschi, Semi-active Electro-inductive devices: characterization and modelling, *Journal of Vibration and Control* 13 (2007) 815–838.
[14] M. Domaneschi, Feasible control solutions of the ASCE benchmark cable-stayed bridge, Structural Control and Health Monitoring, 2009, doi:10.1002/stc.346.
[15] M. Battaini, F. Casciati, M. Domaneschi, Electro-inductive passive and semi-active control devices, *System-based Vision for Strategic and Creative Design (ISEC02)*, Rome, Italy, September 2003, Bontempi, pp. 2085–2090.
[16] F. Zhang, K.M. Grigoriadis, I.J. Fialho, Linear parameter-varying control for active vibration isolation systems with stiffness hysteresis, *Journal of Vibration and Control* 15 (2009) 527–547.
[17] B. Yan, M.J. Brennan, S.J. Elliott, N.S. Ferguson, Active vibration isolation of a system with a distributed parameter isolator using absolute velocity feedback control, *Journal of Sound and Vibration* 10 (2010) 1601–1614.
[18] A.M. Abakumov, G.N. Miatov, Control algorithms for active vibration isolation systems subject to random disturbances, *Journal of Sound and Vibration* 289 (2006) 889–907.
[19] C. Olsson, Active automotive engine vibration isolation using feedback control, *Journal of Sound and Vibration* 294 (2006) 162–176.
[20] K.T. Chen, C.H. Chou, S.H. Chang, Y.H. Liu, Intelligent active vibration control in an isolation platform, *Applied Acoustics* 69 (2008) 1063–1084.
[21] T. Muzuno, T. Furushima, Y. Ishino, M. Takasaki, Realization of a zero-compliance system by using displacement cancellation control, *Journal of Vibration and Control* 16 (2010) 585–599.
[22] S. Suresh, S. Narasimhan, N. Sundararajan, Adaptive control of nonlinear smart base-isolated buildings using Gaussian kernel functions, *Structural Control and Health Monitoring* 15 (2008) 585–603.
[23] N. Zhou, K. Liu, A tunable high-static–low-dynamic stiffness vibration isolator, *Journal of Sound and Vibration* 329 (2010) 1254–1273.
[24] N. Zhou, A Tunable High-static–low-dynamic Stiffness Isolator and Fuzzy-neural Network Based Active Control Isolator, MSc Thesis, Lakehead University, 2009.
[25] I. Stefanini, M. Markovic, Y. Perriard, 3D inductance and impedance determination taking skin effect into account, *IEEE International Conference on Electric Machines and Drives*, 2005, pp. 74–79.
[26] T. Zedler, A. Nikanorov, B. Nacke, Investigation of relative magnetic permeability as input data for numerical simulation of induction surface hardening, *International Scientific Colloquium on Modelling for Electromagnetic Processing*, 2008, pp. 119–126.
[27] D. Zhang, X. Mei, X. Hao, A. Tian, Modeling dynamic magnetic force and robust control, *IEEE International Conference on Systems and Control*, 2007, pp. 349–354.
[28] B. Yan, Active Vibration Isolation with a Distributed Parameter Isolator, PhD Thesis, University of Southampton, 2007.
[29] W.H. Zhu, B. Tryggvason, J.C. Piedboeuf, On active acceleration control of vibration isolation systems, *Control Engineering Practice* 14 (2006) 863–873.
[30] M.Z. Ren, K. Seto, F. Doi, Feedback structure-borne sound control of a flexible plate with an electromagnetic actuator: the phase lag problem, *Journal of Sound and Vibration* 205 (1997) 57–80.
[31] T.H. Wong, Design of a magnetic levitation control system—an undergraduate project, *IEEE Transactions on Education* 29 (1986) 196–200.
[32] J.J. D'Azzo, C.H. Houpis, in: *Linear Control System Analysis and Design*, second ed, McGraw-Hill, New York, 1981.